Langmuir

Article

pubs.acs.org/Langmuir

Nanocrystalline $CeO_{2-\delta}$ as Effective Adsorbent of Azo Dyes

Nataša M. Tomić,[†] Zorana D. Dohčević-Mitrović,*[,†] Novica M. Paunović,[†] Dušan Ž. Mijin,[‡] Nenad D. Radić,[§] Boško V. Grbić,[§] Sonja M. Aškrabić,[†] Biljana M. Babić,[∥] and Danica V. Bajuk-Bogdanović[⊥]

[†]Institute of Physics, University of Belgrade, Pregrevica 118, 11080 Belgrade, Serbia

[‡]Faculty of Technology and Metallurgy, University of Belgrade, Karnegijeva 4, 11000 Belgrade, Serbia

[§]IChTM, Department of Catalysis and Chemical Engineering, University of Belgrade, Njegoševa 12, 11000 Belgrade, Serbia

[∥]Institute of Nuclear Sciences "Vinča", University of Belgrade, 11001 Belgrade, Serbia

[⊥]Faculty of Physical Chemistry, University of Belgrade, Studentski Trg 12-16, 11000 Belgrade, Serbia

Supporting Information

ABSTRACT: Ultrafine $CeO_{2-\delta}$ nanopowder, prepared by a simple and cost-effective self-propagating room temperature synthesis method (SPRT), showed high adsorption capability for removal of different azo dyes. Batch type of adsorption experiments with fixed initial pH value were conducted for the removal of Reactive Orange 16 (RO16), Methyl Orange (MO), and Mordant Blue 9 (MB9). The equilibrium adsorption data were evaluated using Freundlich and Langmuir isotherm models. The Langmuir model slightly better describes isotherm data for RO16 and MO, whereas the Freundlich model was found to best fit the isotherm data for MB9 over the whole concentration range. The maximum adsorption capacities, determined from isotherm data for MO, MB9, and RO16 were 113, 101, and 91 mg g^{-1} respectively. The adsorption process follows the pseudo-second-order kinetic model indicating the coexistence of chemisorption and physisorption. The mechanism of azo dye adsorption is also discussed.

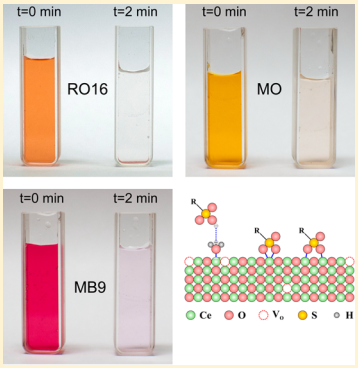

INTRODUCTION

Synthetic dyes are widely used in a number of industries such as textile and leather industries, paper printing, cosmetics, and pharmaceuticals. It is estimated to be more than 10 000 commercially available dyes with over 7×10^5 tons of dyestuff produced annually.[1,2] Azo dyes represent about 60−70% of the dyes used in the textile industry. Some of them show aquatic toxicity or allergenic effects, and under reductive conditions they produce aromatic amines that are carcinogenic.[2,3] Azo dyes represent a class of synthetic, colored, organic compounds, which are characterized by the presence of one or more azo bonds. These dyes belong to the most toxic ones compared to other forms of dyes.[1] Large quantities of these dyes (10−15% of the total world production) are released into the wastewater (typical concentration 10−200 mg L^{-1}), the presence of which poses a major threat to the aquatic organisms as well as animals and humans because of their nonbiodegradability, toxicity, and potential carcinogenic nature.[4−6]

Dye removal from textile effluents is a major environmental problem because of the difficulty to treat such streams by conventional physicochemical and biological treatment methods. The methods such as filtration, coagulation, flocculation, ion exchange, and photocatalytic degradation are unsatisfactory for wastewater treatment because they are expensive and may produce more toxic byproducts. Among the various available water treatment techniques, adsorption is the most reliable and efficient technique for dye removal, despite the fact that usually the adsorbent needs to be regenerated, which increases the cost of the process and can be a time-consuming procedure. The liquid phase adsorption has been shown to be an efficient way for removing the suspended solids, organic matter, and oil from aqueous solutions. Adsorption appears to offer the best perspective over all the other treatments because it can handle fairly large flow rates, producing a high quality effluent and does not result in the formation of harmful substances, such as ozone and free radicals which are present during the photodegradation process using UV.

Activated carbon is the most widely used adsorbent for this purpose, because it has a high surface area and high capacity for adsorption of organic matter, but its use is limited because of its high production cost and significant problems with the regeneration of the spent activated carbon.[7,8] A great variety of low-cost biomass materials[9−13] have been used to produce activated carbon for the treatment of wastewaters. In recent years, low cost agricultural wastes have been investigated as potential biosorbents,[14] but most of these cheap substitutes have to be subjected to the process of carbonization which increases process costs. Therefore, there is still a high demand for cheaper adsorbent materials with high adsorption capacity.

Received: March 6, 2014
Revised: September 8, 2014
Published: September 14, 2014

   dx.doi.org/10.1021/la502969w | *Langmuir* 2014, 30, 11582−11590

Nowadays, nanoscience and nanotechnology play important role in environmental protection. There is a strong need to develop simple and economical methods for producing nanomaterials with higher adsorption rates which can efficiently remove various contaminants. Nanomaterials with high surface area are the most promising candidates as adsorbents in organic dye removal.[5,15−19]

Among various metal oxide semiconductors, CeO_2 is widely used in many application areas such as catalysis, fuel cells, sensors, and UV shielding, owing to its outstanding physical and chemical properties. The application of ceria as effective sorbent is not so often studied. There are few reports in which it is demonstrated that ceria is effective sorbent for the removal of high toxic pollutants such as[17] As(V) and Cr(VI) and azo dyes such as Congo Red[18] or Acid Orange[4] from water. The adsorption experiments, performed to remove Reactive Orange 16 and Methyl Orange from wastewaters, mainly used as adsorbent waste biomass,[20] various types of sludge, and biosorbents.[1,13,14,20−26] Although most of these sorbents were relatively cheap and effective in dye removal, they showed modest and rarely high sorption capacities. On the other side, to the best of our knowledge there is almost no study which concerns the adsorption of Mordant Blue 9.

Herein we present the adsorption capability of ceria nanoparticles for removal of different azo dyes such as Reactive Orange 16, Methyl Orange, and Mordant Blue 9. Ceria nanopowder, obtained by a simple and cost-effective method, has shown very high efficiency toward azo dye removal and has been proven to be a promising alternative for wastewater treatment.

EXPERIMENTAL SECTION

1. Materials Preparation. The ultrafine $CeO_{2-\delta}$ nanopowder was fabricated via a simple and economical self-propagating room temperature synthesis method (SPRT).[27,28] Starting reactants were cerium nitrate hexahydrate ($Ce(NO_3)_3{\cdot}6H_2O$) (Acros Organics 99.5%) and sodium hydroxide (Carlo Erba). Hand-mixing of nitrate with NaOH was performed in alumina mortar for ∼10 min until the mixture turned light brown. After being exposed to air for 4 h, the mixture was suspended in water. Rinsing of $NaNO_3$ was performed in a centrifuge at 3500 rpm for 10 min. This procedure was performed four times with distilled water and twice with ethanol. The precipitate was dried at 60 °C overnight. The reaction based on the self-propagating room temperature method can be written as follows:

$$2[(Ce(NO_3)_3{\cdot}6H_2O] + 6NaOH + (1/2 - \delta)O_2 \rightarrow 2CeO_{2-\delta} + 6NaNO_3 + 15H_2O \quad (1)$$

2. Characterization Methods. X-ray powder diffraction (XRD) data of the sample were collected on a Siemens D-5000 diffractometer with Cu Kα radiation over the 2θ range from 20° to 80°. Atomic force microscope (AFM) images were taken using the Omicron B002645 SPM PROBE VT AFM 25 instrument in noncontact mode at room temperature. The powder specific surface area of the sample was calculated following the multipoint BET procedure on the Quantachrome ChemBet-3000 setup. The pore size distribution was derived from nitrogen adsorption-desorption isotherm obtained at 77 K. The infrared (IR) transmission spectra of $CeO_{2-\delta}$ pellets before and after dye adsorption were measured on a Thermo Nicolet 6700 Fourier transform infrared spectrophotometer at room temperature. Micro-Raman spectra were collected in the backscattering configuration using the TriVista 557 Raman system. The 488 nm line of an Ar^+/Kr^+ mixed gas laser was used as an excitation source. In order to avoid sample heating, the incident laser power on the samples was kept below 20 mW. Surface charge (zeta potential) of ceria nanoparticles at different pH was measured using Zetasizer Nano ZS90 (Malvern Instruments) apparatus. Suspensions were prepared using deionized water as dispersing medium and were ultrasonicated for 15 min prior to the measurements using an ultrasonic bath. The pH values of suspensions were adjusted by adding HCl and NaOH solutions to the starting suspension of $CeO_{2-\delta}$ nanopowder.

3. Adsorption Experiments. The adsorption experiments were carried out as batch tests in a magnetically stirred thermostated glass vessel with three different concentrations (50, 100, and 200 mg L^{-1}) of Reactive Orange 16 (RO16), Methyl Orange (MO), and Mordant Blue 9 (MB9). All measurements were performed at initial pH values of 6.2, 6, and 4.6 for MO, MB9, and RO16 dye solutions, respectively. The suspensions were stirred for 2 min at room temperature in the dark. The adsorption capacity (for the 200 mg L^{-1} concentration of dyes) of coconut-based powdered activated carbon (PAC), of large specific surface area (1200 m^2/g), was determined for comparison. The working volume (25 mL) and the quantity of ceria nanopowders and PAC (50 mg) were kept fixed in all adsorption experiments. At fixed contact time, the samples were taken, centrifuged, and analyzed on a Shimadzu 1700 UV-vis spectrophotometer within the spectral range where maximum absorption for each dye occurs. In Table S1 (see the Supporting Information) are given the chemical structure and the wavelength of maximal absorption (λ_{max}) for each dye.

RESULTS AND DISCUSSION

The powder XRD pattern of $CeO_{2-\delta}$ nanopowder is presented in Figure 1a. Diffraction peaks corresponding to cubic fluorite structure are clearly observed. All XRD peaks are broadened, indicating that the crystallite size is within the nanometer range. The average size of $CeO_{2-\delta}$ nanocrystals, estimated by the Wiliamson-Hall method,[29] is about 6 nm. The noncontact AFM image of $CeO_{2-\delta}$ sample (Inset of Figure 1b) shows small and agglomerated nonporous $CeO_{2-\delta}$ particles. The pores between agglomerated $CeO_{2-\delta}$ nanoparticles are also visible on the AFM image. Particle size distribution obtained from the AFM image of $CeO_{2-\delta}$ sample is presented in Figure 1b, and it was modeled by asymmetric double sigmoidal function. The average particle size is 11.4 nm.

To determine the surface area and pore size distribution, nitrogen adsorption−desorption isotherms at 77 K were recorded, and these are given in the inset of Figure 1c. According to the IUPAC classification,[30] the nitrogen adsorption−desorption isotherm is attributed to the Langmuir IV type. The pore size distribution was determined from the desorption branch of the isotherms using the BJH (Barrett−Joyner−Halenda) method and is shown in Figure 1c. It can be observed that the sample has bimodal pore size distribution in the mesoporous area with the first mode peak around 2 nm and the second one in the range 3−4 nm. The value of the BET specific surface area (S_{BET}) is 74 m^2 g^{-1}.

Further, we examined the performances of $CeO_{2-\delta}$ nanopowder as a potential adsorbent for removal of RO16, MO, and MB9. The adsorption measurements were carried out with three different concentrations of the dye solutions (50, 100, and 200 mg L^{-1}), and absorption spectra of the dye solutions were collected after certain time intervals. The UV−vis spectrum of RO16 is given in Figure 2a (blue line) for the concentration of 50 mg L^{-1}. The absorption spectrum of RO16 in the presence of $CeO_{2-\delta}$ nanoparticles after 2 min is also presented in Figure 2a (red line). As can be seen, the RO16 characteristic bands decreased promptly, indicating that RO16 was removed from the solution. The corresponding photo image (right panel of Figure 2a) shows that the solution is almost colorless. The absorption spectra of the MO and MB9 before (blue line) and after 2 min (red line) in the presence of $CeO_{2-\delta}$ nanoparticles are given in Figure 2b,c. Absorption spectra of these two dye

dx.doi.org/10.1021/la502969w | Langmuir 2014, 30, 11582−11590

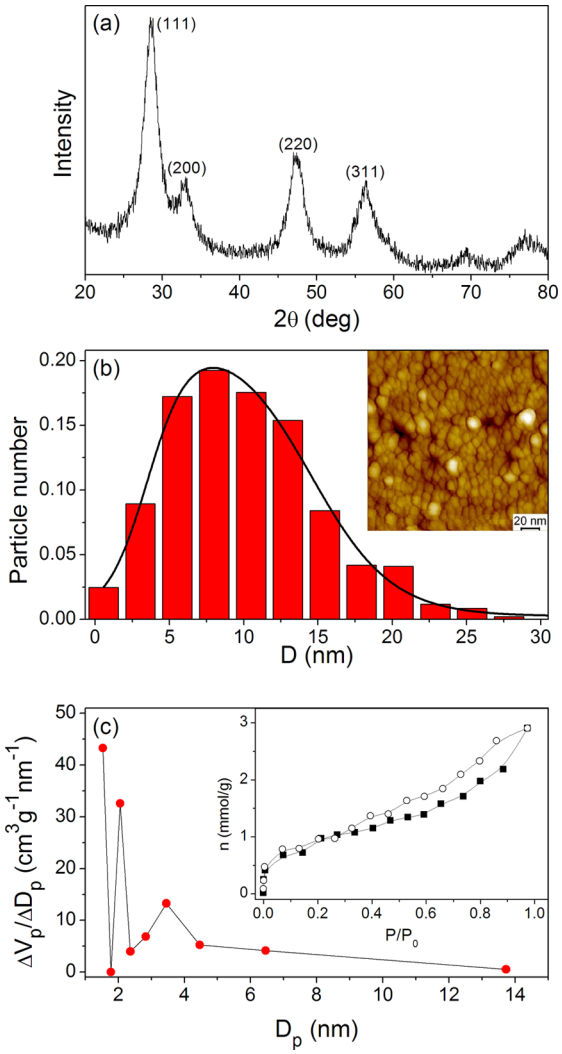

Figure 1. XRD spectrum (a), particle size distribution obtained from AFM (b), and pore size distribution curve obtained from the desorption branch of the isotherm (c) for $CeO_{2-\delta}$ nanopowder. Insets present the AFM image and the nitrogen adsorption–desorption isotherm of $CeO_{2-\delta}$ nanopowder.

solutions after 2 min showed that the dyes were present in a very low concentration. From the photo images (right panel of Figure 2b,c), it can be noticed that the solutions were almost colorless after 2 min. The experiment was repeated with an increased concentration for all three dyes (100 mg L^{-1}), and the obtained results were similar.

The concentration of RO16 in the solution was further increased to 200 mg L^{-1}. The absorption spectra of RO16 dye solution in the presence of $CeO_{2-\delta}$ nanoparticles, presented in Figure S1a (Supporting Information), demonstrate that $CeO_{2-\delta}$ quickly removes the RO16 from the solution. After 40 min, the equilibrium state was reached. The adsorption measurements were also performed on the solutions of MO and MB9 (200 mg L^{-1}) in the presence of $CeO_{2-\delta}$ nanopowder, in order to compare the efficiency of adsorption process onto ceria nanopowder for all three dyes. The adsorption capacity of $CeO_{2-\delta}$ nanopowder was determined from the mass balance relationship:[1,13,15,22]

$$q_e = \frac{(C_0 - C_e)V}{m} \quad (2)$$

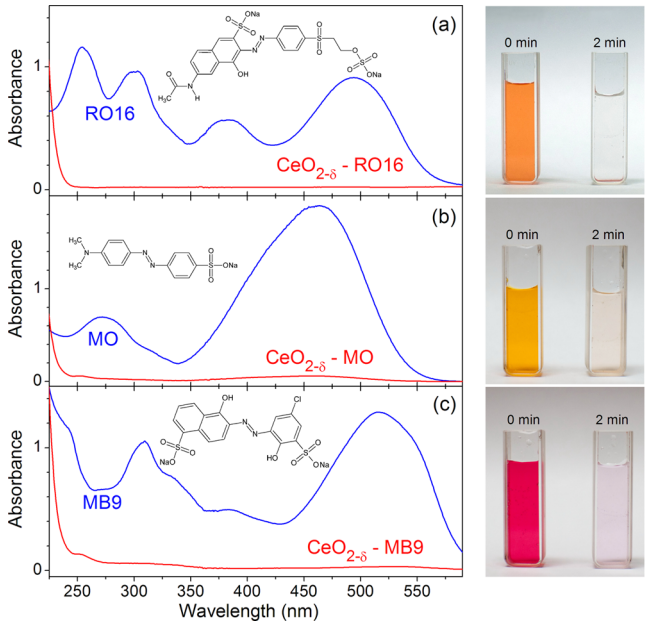

Figure 2. Absorption spectra with corresponding photo images of (a) RO16, (b) MO, and (c) MB9 dye solutions (50 mg L^{-1}) before and 2 min after introducing $CeO_{2-\delta}$ nanoparticles (2 g L^{-1}). Mass of adsorbent = 50 mg; solution volume = 25 mL.

where q_e represents the amount of dye adsorbed per unit mass of adsorbent (mg g^{-1}), C_0 and C_e are the initial and equilibrium liquid phase concentrations (mg L^{-1}), respectively, V is the volume of the solution (L), and m is the mass (g) of $CeO_{2-\delta}$ used.

The adsorption rate and the amount of adsorbed dye with contact time for the solutions of RO16, MO, and MB9 (200 mg L^{-1}) are illustrated in Figure 3a,b. As can be noticed from Figure 3, for all three curves, it is characteristic that the adsorption process is rapid in the initial stage, whereas in the later stage it becomes much slower. The adsorption rate for RO16 was higher at the beginning, but after 60 min much better elimination of MO from the solution was observed, whereas the adsorption rate of MB9 was still lower. The equilibrium was achieved after 40 (60) min for RO16 (MO), whereas for MB9 it was achieved after 180 min. The adsorption capacities of $CeO_{2-\delta}$ nanopowder in the case of MO, MB9, and RO16 were 100, 94, and 91 mg g^{-1}, respectively.

Further, the adsorption capacities of $CeO_{2-\delta}$ nanopowder and activated carbon were compared. The adsorption capacity of commercial activated carbon (50 mg) is presented in Figure 4 for MO (a) , RO16 (b), and MB9 (c) solutions (200 mg L^{-1}). In the case of MO dye solution, it can be noticed that at the beginning of the adsorption process the activated carbon was slightly faster than $CeO_{2-\delta}$ nanopowder and reached the equilibrium state after 20 min. After 60 min, both curves overlapped. In the case of RO16 dye solution, activated carbon was much slower compared to $CeO_{2-\delta}$. After 40 min, $CeO_{2-\delta}$ nanopowder reached equilibrium and eliminated almost 90% of RO16 from the solution, whereas activated carbon needed 2 h to reach the final adsorption capacity of 85 mg g^{-1} which was still lower than that of ceria nanopowder (91 mg g^{-1}). The adsorption capability of $CeO_{2-\delta}$ for MB9 is lower than that for activated carbon, although after 2 h the final adsorption capacities were comparable.

dx.doi.org/10.1021/la502969w | Langmuir 2014, 30, 11582–11590

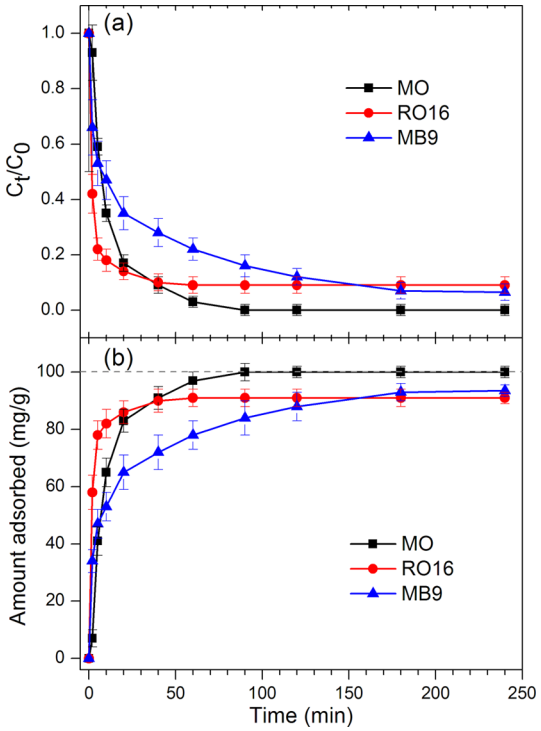

Figure 3. Adsorption rate (a) and amount of adsorbed dyes (b) for the solutions of MO, RO16, and MB9 (200 mg L^{-1}) in the presence of $CeO_{2-\delta}$ nanopowder. Mass of adsorbent = 50 mg; solution volume = 25 mL.

In Figure 5a–c are shown the IR transmission spectra of pure dyes and $CeO_{2-\delta}$ nanopowders after dye adsorption. For comparison, the IR spectrum of pure $CeO_{2-\delta}$ nanopowder is also given in Figure 5a–c.

The IR spectra of pure dyes have some common characteristic bands.[4,6,31−36] The bands at 1040/1120 cm^{-1} in MO, 1054/1139 cm^{-1} in RO16, and 1044/1136 cm^{-1} in MB9 originate from the symmetric stretching vibrations of the SO_3^- group ($\nu_s(SO_3^-)$). The band at 1204 cm^{-1} in MO, 1236 cm^{-1} in RO16, and 1190 cm^{-1} in MB9 represents the asymmetric stretching vibrations of the SO_3^- group ($\nu_{as}(SO_3^-)$). The band at 1368 cm^{-1} in MO and 1372 cm^{-1} in RO16 belongs to the C–N stretching vibrations. The bands at 1422, 1410, and 1409 cm^{-1} in MO, RO16, and MB9, respectively, are assigned to the N=N stretching vibrations. The bands at 1520/1608 cm^{-1} in MO and 1586 cm^{-1} in RO16 are from the aromatic ring stretching vibrations. The band at 1672 cm^{-1} in the spectra of RO16 originates from the stretching vibrations of the carbonyl C=O group.

In the IR spectrum of MO dye adsorbed on $CeO_{2-\delta}$ (shown in Figure 5a), the IR bands of the MO dye are of much lower intensity. The pronounced changes of the IR bands characteristic for sulfonate stretching vibration mode are observed. The $\nu_{as}(SO_3^-)$ band at 1204 cm^{-1} is much weaker after MO adsorption on $CeO_{2-\delta}$ and shifted to ∼1193 cm^{-1} (marked with arrow in Figure 5a). The $\nu_s(SO_3^-)$ band at 1040 cm^{-1} in MO is slightly shifted to 1034 cm^{-1} (marked with arrow in Figure 5a) in the CeO_2–MO spectrum, the intensity of which is much lower after adsorption. All these changes can indicate that the sulfonate group is strongly involved in the adsorption of MO onto $CeO_{2-\delta}$.[34] In the IR spectrum of RO16 adsorbed onto $CeO_{2-\delta}$ (Figure 5b), a significant intensity decrease of the IR bands at 1054/1139 and 1500 cm^{-1}, characteristic for SO_3^-

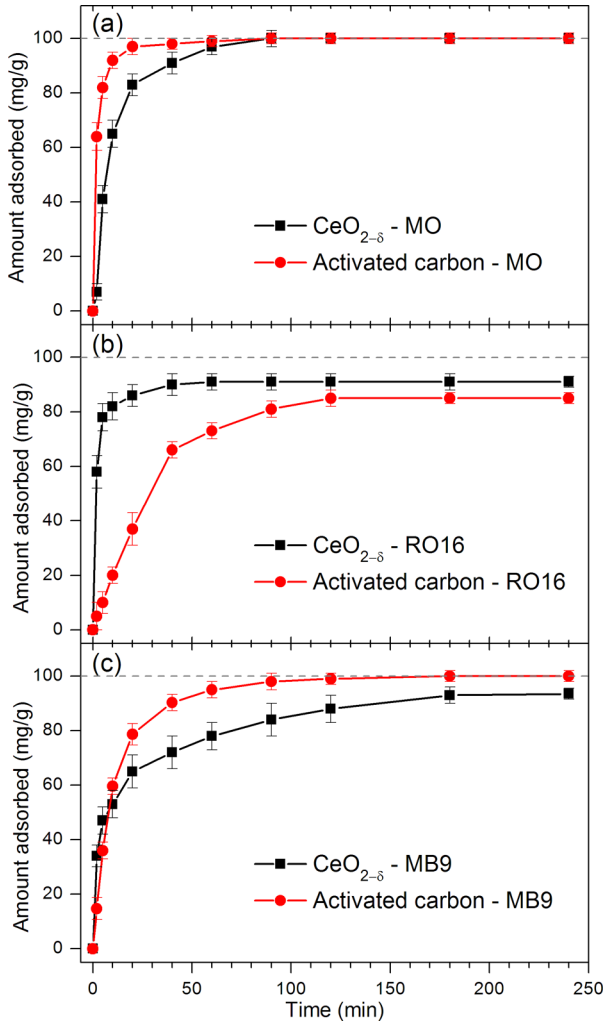

Figure 4. Comparison of adsorption capacities between $CeO_{2-\delta}$ nanopowder and activated carbon in the case of (a) MO, (b) RO16, and (c) MB9 dye solutions (200 mg L^{-1}). Mass of adsorbent = 50 mg; solution volume = 25 mL.

group and N–H bending vibrations,[4,6] is observed too. Many other bands which belong to pure RO16 dye are much weaker or barely visible in the $CeO_{2-\delta}$–RO16 spectrum, as for instance the band at 1410 cm^{-1} for N=N stretching vibrations. The carbonyl C=O peak at 1672 cm^{-1} in the IR spectrum of RO16, is almost absent from the $CeO_{2-\delta}$–RO16 spectrum. The $\nu_s(SO_3^-)$ band is shifted from 1139 to 1136 cm^{-1} in the $CeO_{2-\delta}$–RO16 spectrum. In the IR spectrum of $CeO_{2-\delta}$–MB9 (Figure 5c), a major decrease of the MB9 band intensity is observed and the slight shift of the asymmetric $\nu_s(SO_3^-)$ band is barely visible (marked with arrow in Figure 5c). All this indicates that RO16 and MB9 are also strongly adsorbed onto the $CeO_{2-\delta}$ surface. In Figure 5d is presented the IR transmission spectrum of pure $CeO_{2-\delta}$ in the extended spectral range. As can be seen, strong bands near 3400 and 1620 cm^{-1} are attributed to the adsorbed H_2O and hydroxyls.[37,38] The absorption band at 1384 cm^{-1} originates from CO_2 molecule vibrations.

Raman spectra, obtained on $CeO_{2-\delta}$ nanopowder before and after dye adsorption, are presented in Figure 6 and are consistent with the IR measurements. In the Raman spectra of nanocrystalline $CeO_{2-\delta}$ treated with dyes, besides the F_{2g} mode of pure $CeO_{2-\delta}$ positioned at ∼456.5 cm^{-1} and the mode at

dx.doi.org/10.1021/la502969w | *Langmuir* 2014, 30, 11582−11590

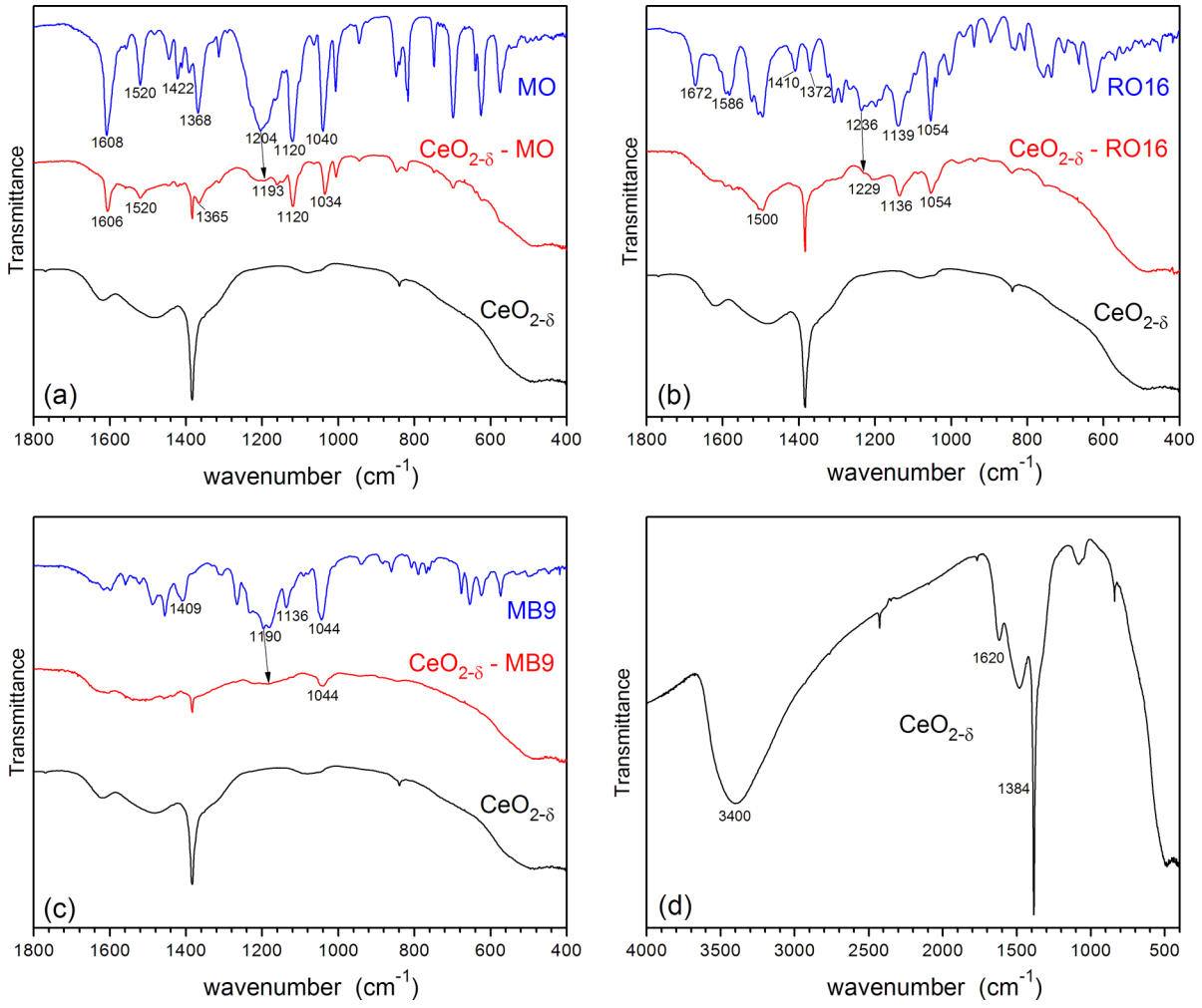

Figure 5. IR transmission spectra of (a) MO, (b) RO16, and (c) MB9 adsorbed on $CeO_{2-\delta}$ together with the transmission spectra of pure dyes and $CeO_{2-\delta}$ nanopowder. (d) IR transmission spectrum of $CeO_{2-\delta}$ nanopowder in the extended range.

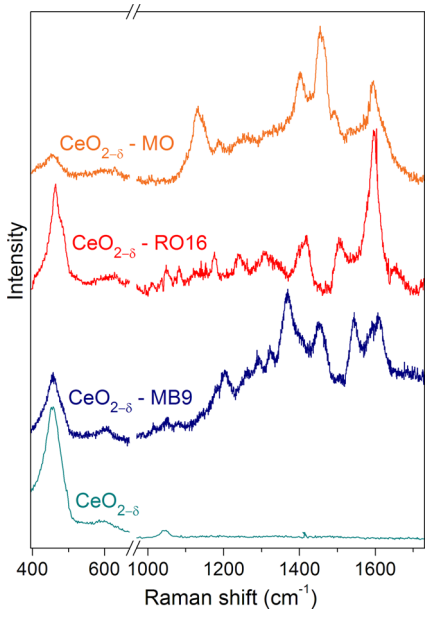

Figure 6. Room temperature Raman spectra of $CeO_{2-\delta}$ nanopowder before and after adsorption of MO, RO16, and MB9 dyes.

~600 cm^{-1} which belongs to intrinsic oxygen vacancies,[39] additional modes are observed. These new modes correspond to the vibrations of different atomic groups of dye molecules, such as −N═N−, −C═O, −S═O, −O−H, and aromatic ring vibrations. The most prominent mode frequencies deduced from the spectra of ceria treated with MO, RO16, and MB9 are summarized in the Table S2 (see the Supporting Information). As the majority of the atomic group vibrations characteristic for the dye molecules in question are observed in the Raman spectra of dyed ceria nanopowder, it can be concluded that in all three cases the adsorption of dye molecules took place.

The IR and Raman spectra unambiguously showed that MO, RO16, and MB9 are adsorbed on $CeO_{2-\delta}$ surface. In addition, from the IR spectra of three azo dyes adsorbed on $CeO_{2-\delta}$ nanopowders, we concluded that ν_{as} and ν_s bands of sulfonate groups are affected considerably. The intensity ratio of these bands ($\nu_{as}(SO_3^-)/\nu_s(SO_3^-)$ = 0.4) for adsorbed MO onto ceria is different from the same ratio in the spectrum of isolated MO ($\nu_{as}(SO_3^-)/\nu_s(SO_3^-)$ = 0.9). The changes of the ν_{as} and ν_s band intensities of sulfonate groups are also registered in the IR spectra of adsorbed RO16 and MB9 onto ceria. It is further worth mentioning that the frequency difference $\Delta\nu_{as\text{-}s}$ ($\nu_{as}(SO_3^-) - \nu_s(SO_3^-)$) in the MO, RO16, and MB9 spectra is higher than that in the corresponding spectra of adsorbed dyes on ceria (see Figure 5). This is characteristic of the

dx.doi.org/10.1021/la502969w | Langmuir 2014, 30, 11582−11590

bidentate type coordination according to the Deacon and Phillips[40] empirical rule and the work of Bauer et al.,[41] formed when OH groups situated on the surface metal cations are substituted with oxygen atoms from azo dyes. Ji et al.[4] noticed similar changes to ours in the IR spectra of acid orange adsorbed onto CeO_2 surface and proposed that a bidentate type bridge is formed between sulfonate group and Ce^{4+} cations. According to the observed changes in the IR spectra of MO, RO16, and MB9 adsorbed on $CeO_{2-\delta}$ nanopowder, it is reasonable to assume that all three dyes form a bidentate type bridge on the ceria surface, where two oxygen atoms of the SO_3^- group are bound to one or two Ce^{4+} cations in a process that involves the substitution of surface coordinated OH groups on Ce^{4+} cations with oxygen atoms from azo dyes.

Another very important factor for dye removal concerns the capability of $CeO_{2-\delta}$ nanopowders to easily form oxygen vacancies on the surface which accompany functional groups. The surface functional groups can interact with dye molecules via hydrogen bonds and/or electrostatic forces promoting the adsorption of dye molecules. The first principle density functional theory calculations performed by Yang et al.[42] have shown that, in oxygen deficient ceria, the adsorbed water molecules prefer to decompose near the oxygen vacancy site, forming surface hydroxyls, where H atoms are bonded with surface oxygen atoms. Therefore, they concluded that in reduced ceria both adsorbed H_2O and surface hydroxyls coexist. Their calculations are in good agreement with experimental work of Kundakovic et al.[43] performed on oxidized and reduced CeO_2 thin films, who detected surface hydroxyls only in reduced ceria films.

Having in mind that our ceria is oxygen deficient, it is reasonable to assume that hydroxyl groups, already observed in the IR spectra, are present on the surface of $CeO_{2-\delta}$ nanopowder. The experimental determination of the pH value at zero point charge (pH_{ZPC}) revealed that $CeO_{2-\delta}$ has pH_{ZPC} = 6.3 (Figure S2 in the Supporting Information). As pH values of the dye solutions are lower than pH_{ZPC} of $CeO_{2-\delta}$ (see section 3 in Experimental Section), $CeO_{2-\delta}$ as adsorbent acts as a positive surface. The electrostatic attraction between ceria nanoparticles and negatively charged dye ions is an operable mechanism. In that case, the ceria surface hydroxyls are protonated:

$$Ce{-}OH + H^+ \rightarrow Ce{-}OH_2^+ \quad (3)$$

In aqueous solution, the sulfonate groups ($R{-}SO_3Na$) dissociate and are converted to anionic dye ions. The adsorption process further proceeds due to the electrostatic attraction between these two oppositely charged ions:

$$Ce{-}OH_2^+ + R{-}SO_3^- \rightleftarrows Ce{-}OH_2^+ \cdots {}^-O_3S{-}R \quad (4)$$

Illustration of the adsorption mechanisms between dye molecules and $CeO_{2-\delta}$ adsorbent is shown in Figure 7.

As we stated earlier, the adsorption rate at the beginning of the process (presented in Figure 3a) is higher for RO16 than for MO and MB9. The difference in removal efficiency between three dyes can be explained by the fact that the pH value of the RO16 solution is close to the pH value where ceria net positive charge surface has maximum, whereas the pH values of MO and MB9 dye solutions are close to the pH_{ZPC} value of $CeO_{2-\delta}$. Therefore, the electrostatic interaction between RO16 dye molecules and $CeO_{2-\delta}$ at the beginning will be stronger than that for MB9 and MO. It is important to emphasize that

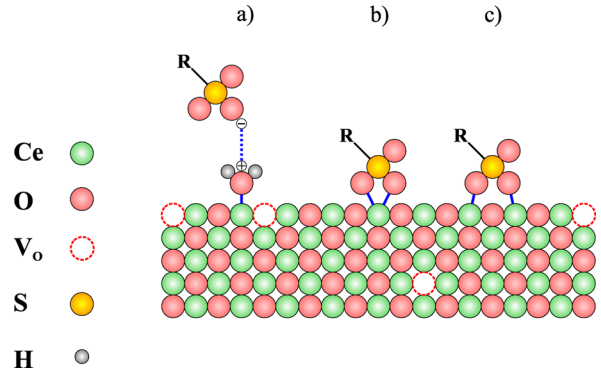

Figure 7. Schematic representation of RO16, MO, and MB9 adsorption on $CeO_{2-\delta}$ surface. (a) Electrostatic interaction between protonated ceria surface and sulfonate group in the dye molecule; (b, c) bidentate type structures between sulfonate group and Ce^{4+} cations.

sulfonic groups, which dissociate in aqueous solution and convert to $R{-}SO_3^-$ anions, are negatively charged even at higher acidic solutions, because their pK_a values are lower than zero.[44] Finally, the interaction between OH groups on the surface of $CeO_{2-\delta}$ and NH groups of the RO16 is also a possible mechanism for RO16 dye adsorption[19] and can explain the higher adsorption rate in the case of RO16 at the beginning of the process.

The study of the adsorption equilibrium isotherm is helpful in determining the maximum adsorption capacity of adsorbent for given adsorbate. These isotherms relate the dye uptake per unit mass of adsorbent, q_e, to the equilibrium liquid phase concentration C_e. In Figure 8 are presented the adsorption isotherms for RO16 (a), MO (b), and MB9 (c) dye solutions, measured at room temperature. Adsorption isotherms were analyzed according to Langmuir and Freundlich models in order to determine the best-fit model. Langmuir's model predicts the monolayer coverage of the adsorbate, assuming that all adsorption sites are identical and energetically equivalent, whereas the Freundlich's model assumes the adsorption on heterogeneous surface composed of nonidentical adsorption sites with different energy of adsorption. The isotherm equations and isotherm parameters for both models are listed in Supporting Information Table S3.

The adsorption isotherms of RO16 and MO from Figure 8a,b can be fitted by both the Langmuir and Freundlich equations. Both models give reasonable good fit in the case of MO and RO16, although the values of correlation coefficients (Supporting Information Table S3) are slightly higher for the Langmuir isotherm. The sorption data of MB9 are much better represented by the Freundlich model (Figure 8c and Supporting Information Table S3) which expresses adsorption in a multilayer manner on an energetically heterogeneous surface.

The parameter $1/n$ from the Freundlich equation characterizes the heterogeneity of the site energies and the adsorption intensity, that is, the degree of nonlinearity of adsorption isotherm. In their work, Tseng and Wu[45] have defined a favorable level for the adsorption isotherm curves and gave a classification for the values of parameter $1/n$. Despite the fact that the Langmuir model seems more suitable to describe the sorption of MO and RO16 onto ceria, according to Tseng's classification, the parameter $1/n$ (listed in Supporting Information Table S3) lies in the range of strongly favorable (for RO16 and MO) and favorable (for MB9) adsorption.

dx.doi.org/10.1021/la502969w | Langmuir 2014, 30, 11582−11590

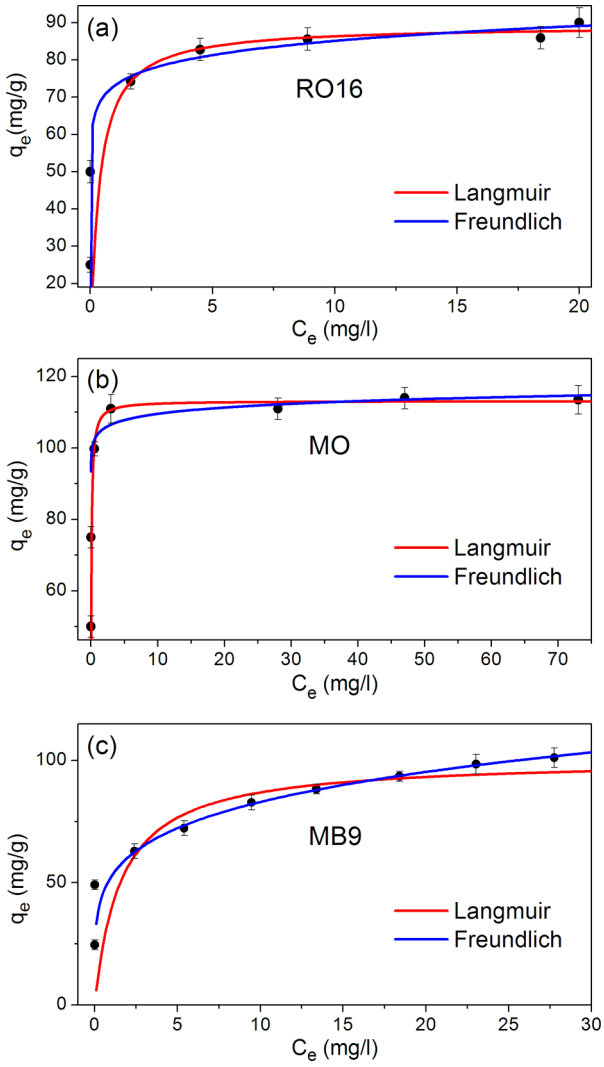

Figure 8. Adsorption isotherms of (a) RO16, (b) MO, and (c) MB9 dye solutions on $CeO_{2-\delta}$ at room temperature. Initial dye concentration = 50–230 mg L^{-1}; mass of adsorbent = 50 mg; solution volume = 25 mL.

Therefore, keeping in mind that oxygen-deficient surface of nanosized ceria is more heterogeneous than homogeneous, it is reasonable to conclude that adsorption of MB9, MO, and RO16 on $CeO_{2-\delta}$ nanopowders reflects the presence of more than one kind of adsorbent–adsorbate surface interaction. The maximal adsorption capacity values of $CeO_{2-\delta}$ nanopowder from isotherm data were found to be 113, 101, and 91 mg g^{-1} in the case of MO, MB9, and RO16 respectively.

To get further insight into the mechanism of adsorption, pseudo-first- and pseudo-second-order models were used to simulate the adsorption data for various contact times from Figure 3b. The pseudo-first-order model didn't give a good fit of the experimental data and will be omitted in further discussion. Kinetic data were further analyzed with the pseudo-second-order kinetic model shown in Figure 9. The linear form of the pseudo-second-order model is expressed as follows:

$$\frac{t}{q_t} = \frac{1}{k_2 q_e^{\,2}} + \frac{t}{q_e} \tag{4}$$

where q_e and q_t refer to the amount of adsorbed dye at equilibrium and at time t, respectively, and k_2 is the equilibrium

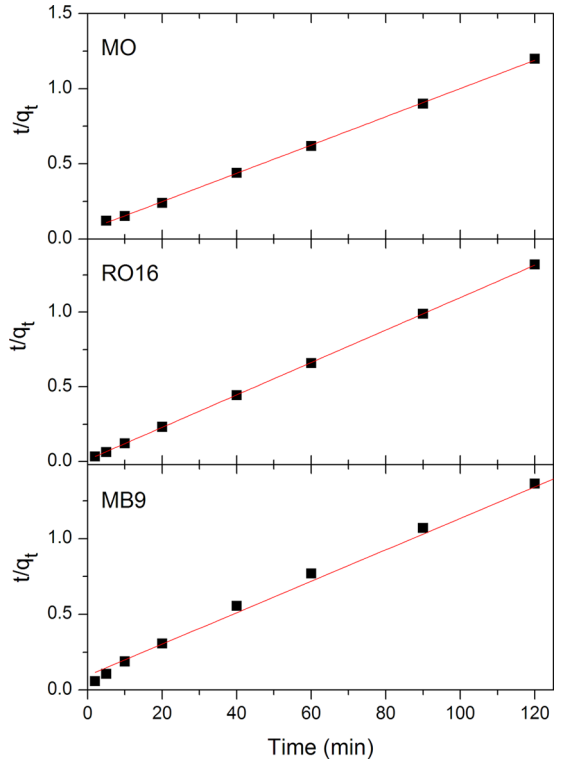

Figure 9. Pseudo-second-order kinetics of MO, RO16, and MB9 onto $CeO_{2-\delta}$ nanopowder. Initial dye concentration = 200 mg L^{-1}; mass of adsorbent = 50 mg; solution volume = 25 mL.

rate constant of the pseudo-second-order kinetic model. The linear plots of t/q_t vs t (Figure 9) show that the experimental data agree well with the pseudo-second-order kinetic model for all three dyes. The values of q_e and k_2 were calculated from the slope and intercept of eq 4, and their values are given in Table 1, together with experimental q_e values and correlation

Table 1. Pseudo-Second-Order Kinetic Model Parameters Together with Experimental q_e Values for Adsorption of Each Dye

	$q_{e,cal}$ (mg g^{-1})	$q_{e,exp}$ (mg g^{-1})	k_2 (g mg^{-1} min^{-1})	R^2
MO	106.3	100	1.44×10^{-3}	0.9994
RO16	100	91	9.09×10^{-3}	0.9999
MB9	96.3	93.6	1.13×10^{-3}	0.9977

coefficients. Calculated q_e values, tabulated in Table 1, are in quite good agreement with experimental ones and the correlation coefficients have large values ($R^2 > 0.99$). It can be concluded that the adsorption of MO, RO16, and MB9 on $CeO_{2-\delta}$ nanopowder follows the pseudo-second-order kinetic model which relies on the assumption that chemisorption and effective electrostatic interactions play a major role in the adsorption process.[46,47] Comparing the adsorption capacities of $CeO_{2-\delta}$ nanopowder with other adsorbents mentioned in the Introduction, we can conclude that $CeO_{2-\delta}$ nanopowder, produced by cost-effective SPRT method, shows efficient adsorption properties and is a promising candidate for environmentally friendly adsorbents in water treatment.

CONCLUSIONS

The $CeO_{2-\delta}$ nanopowder, synthesized by a facile and cost-effective SPRT method, appeared to be a very effective sorbent

dx.doi.org/10.1021/la502969w | Langmuir 2014, 30, 11582–11590

for the MO, RO16, and MB9 azo dyes. The adsorption process was monitored at fixed initial pH value and varying dye concentration and contact time. Infrared and Raman spectroscopy measurements confirmed that the adsorption of azo dyes on the $CeO_{2-\delta}$ surface took place. The experimental adsorption data for the MO and RO16 were slightly better fitted with the Langmuir isotherm, whereas the Freundlich isotherm was a better fit for MB9 over the whole concentration range. According to the values of the Freundlich constant ($1/n$), the adsorption of MB9, MO, and RO16 lies in a favorable and strongly favorable zone. The highest adsorption capacity of $CeO_{2-\delta}$ was obtained for MO (113 mg g^{-1}) and then for MB9 (101 mg g^{-1}) and RO16 (91 mg g^{-1}). The formation of a bidentate type bridge between sulfonate group and Ce^{4+} cations and the protonation of ceria surface hydroxyls can be responsible for effective adsorption process. Adsorption of MO, RO16, and MB9 dyes follows the pseudo-second-order equation with good correlation. These results imply that, besides strong electrostatic sorption, chemisorption mechanism may play an important role for the dye adsorption. Based on our results, ceria nanopowder prepared by the SPRT method represents an effective dye adsorbent and can be a promising substitute in wastewater treatment.

■ ASSOCIATED CONTENT

Supporting Information

Figures showing absorption spectra of RO16 (200 mg L^{-1}) and photo image of RO16 solutions in the presence of $CeO_{2-\delta}$ nanopowders, and zeta potential of $CeO_{2-\delta}$ nanoparticles. Tables showing dye structures and their wavelengths of maximal absorption, values of the Raman shifts extracted from the experimental Raman spectra of $CeO_{2-\delta}$ nanopowder after adsorption of MO, RO16, and MB9, and isotherm equations and parameters for azo dyes at room temperature. This material is available free of charge via the Internet at http://pubs.acs.org.

■ AUTHOR INFORMATION

Corresponding Author

*E-mail: zordoh@ipb.ac.rs.

Notes

The authors declare no competing financial interest.

■ ACKNOWLEDGMENTS

We thank Bojan R. Stojadinović for the AFM image and Bojan Čalija for the zeta potential measurements. This work was financially supported by the Serbian Ministry of Education, Science and Technological Development under Projects ON171032 and III45018 and bilateral Project Serbia-Italy No. RS13MO11.

■ REFERENCES

(1) Lee, J. W.; Choi, S. P.; Thiruvenkatachari, R.; Shim, W. G.; Moon, H. Evaluation of the performance of adsorption and coagulation processes for the maximum removal of reactive dyes. *Dyes Pigm.* **2006**, *69*, 196−203.

(2) Gomez, V.; Larrechi, M. S.; Callao, M. P. Kinetic and adsorption study of acid dye removal using activated carbon. *Chemosphere* **2007**, *69*, 1151−1158.

(3) Silva, J. P.; Sousa, S.; Rodrigues, J.; Antunes, H.; Porter, J. J.; Goncalves, I.; Ferreira-Dias, S. Adsorption of acid orange 7 dye in aqueous solutions by spent brewery grains. *Sep. Purif. Technol.* **2004**, *40*, 309−315.

(4) Ji, P. F.; Zhang, J. L.; Chen, F.; Anpo, M. Study of adsorption and degradation of acid orange 7 on the surface of CeO_2 under visible light irradiation. *Appl. Catal., B* **2009**, *85*, 148−154.

(5) Venkatesha, T. G.; Viswanatha, R.; Nayaka, Y. A.; Chethana, B. K. Kinetics and thermodynamics of reactive and vat dyes adsorption on MgO nanoparticles. *Chem. Eng. J.* **2012**, *198*, 1−10.

(6) Sahasrabudhe, M.; Pathade, G. Biodegradation of azo dye C.I. Reactive Orange 16 by an actinobacterium Georgenia sp. CC-NMPT-T3. *Int. J. Adv. Res.* **2013**, *1*, 91−99.

(7) Mohan, D.; Pittman, C. U., Jr Activated carbons and low cost adsorbents for remediation of tri- and hexavalent chromium from water. *J. Hazard. Mater.* **2006**, *137*, 762−811.

(8) Pollard, S. J. T.; Fowler, G. D.; Sollars, C. J.; Perry, R. Low-cost adsorbents for waste and wastewater treatment: a review. *Sci. Total Environ.* **1992**, *116*, 31−52.

(9) Amin, N. K. Removal of direct blue-106 dye from aqueous solution using new activated carbons developed from pomegranate peel: Adsorption equilibrium and kinetics. *J. Hazard. Mater.* **2009**, *165*, 52−62.

(10) Sharma, Y. C.; Uma; Upadhyay, S. N. Removal of a cationic dye from wastewaters by adsorption on activated carbon developed from coconut coir. *Energy Fuels* **2009**, *23*, 2983−2988.

(11) Aygün, A.; Yenisoy-Karakaş, S.; Duman, I. Production of granular activated carbon from fruit stones and nutshells and evaluation of their physical, chemical and adsorption properties. *Microporous Mesoporous Mater.* **2003**, *66*, 189−195.

(12) Kannan, N.; Sundaram, M. M. Kinetics and mechanism of removal of methylene blue by adsorption on various carbons—a comparative study. *Dyes Pigm.* **2001**, *51*, 25−40.

(13) Annadurai, G.; Juang, R. S.; Lee, D. J. Use of cellulose-based wastes for adsorption of dyes from aqueous solutions. *J. Hazard. Mater.* **2002**, *92*, 263−274.

(14) Haddadian, Z.; Shavandi, M. A.; Abidin, Z. Z.; Fakhru'l-Razi, A.; Ismail, M. H. S. Removal methyl orange from aqueous solutions using dragon fruit (Hylocereusundatus) foliage. *Chem. Sci. Trans.* **2013**, *2*, 900−910.

(15) Cheung, W. H.; Szeto, Y. S.; Mckay, G. Enhancing the adsorption capacities of acid dyes by chitosan nano particles. *Bioresour. Technol.* **2009**, *100*, 1143−1148.

(16) Wu, C. H. Adsorption of reactive dye onto carbon nanotubes: Equilibrium, kinetics and thermodynamics. *J. Hazard. Mater.* **2007**, *144*, 93−100.

(17) Zhong, L. S.; Hu, J. S.; Cao, A. M.; Liu, Q.; Song, W. G.; Wan, L. J. 3D flowerlike ceria micro/nanocomposite structure and its application for water treatment and CO removal. *Chem. Mater.* **2007**, *19*, 1648−1655.

(18) Ouyang, X. W.; Li, W.; Xie, S. L.; Zhai, T.; Yu, M. H.; Gan, J. Y.; Lu, X. H. Hierarchical CeO_2 nanospheres as highly-efficient adsorbents for dye removal. *New J. Chem.* **2013**, *37*, 585−588.

(19) Zhai, T.; Xie, S. L.; Lu, X. H.; Xiang, L.; Yu, M. H.; Li, W.; Liang, C. L.; Mo, C. H.; Zeng, F.; Luan, T. G.; Tong, Y. X. Porous $Pr(OH)_3$ nanostructures as high-efficiency adsorbents for dye removal. *Langmuir* **2012**, *28*, 11078−11085.

(20) Won, S. W.; Yun, H. J.; Yun, Y.-S. Effect of pH on the binding mechanisms in biosorption of Reactive Orange 16 by Corynebacterium glutamicum. *J. Colloid Interface Sci.* **2009**, *331*, 83−89.

(21) Won, S. W.; Choi, S. B.; Yun, Y.-S. Performance and mechanism in binding of Reactive Orange 16 to various types of sludge. *Biochem. Eng. J.* **2006**, *28*, 208−214.

(22) Janaki, V.; Vijayaraghavan, K.; Ramasamy, A. K.; Lee, K. J.; Oh, B. T.; Kamala-Kannan, S. Competitive adsorption of Reactive Orange 16 and Reactive Brilliant Blue R on polyaniline/bacterial extracellular polysaccharides composite-A novel eco-friendly polymer. *J. Hazard. Mater.* **2012**, *241*, 110−117.

(23) Suteu, D.; Zaharia, C.; Malutan, T. Removal of orange 16 reactive dye from aqueous solutions by waste sunflower seed shells. *J. Serb. Chem. Soc.* **2011**, *76*, 17.

(24) Zhao, D.; Zhang, W.; Chen, C.; Wang, X. Adsorption of Methyl Orange dye onto multiwalled carbon nanotubes. *Procedia Environ. Sci.* **2013**, *18*, 890−895.
(25) Saha, T. K.; Bhoumik, N. C.; Karmaker, S.; Ahmed, M. G.; Ichikawa, H.; Fukumori, Y. Adsorption of Methyl Orange onto Chitosan from Aqueous Solution. *J. Water Resour. Prot.* **2010**, *2*, 8.
(26) Ai, L.; Zhang, C.; Meng, L. Adsorption of Methyl Orange from Aqueous Solution on Hydrothermal Synthesized Mg−Al Layered Double Hydroxide. *J. Chem. Eng. Data* **2011**, *56*, 4217−4225.
(27) Yu, X.; Li, F.; Ye, X.; Xin, X.; Xue, Z. Synthesis of cerium(IV) oxide ultrafine particles by solid-state reactions. *J. Am. Ceram. Soc.* **2000**, *83*, 964−966.
(28) Boskovic, S.; Djurovic, D.; Dohcevic-Mitrovic, Z.; Popovic, Z.; Zinkevich, M.; Aldinger, F. Self-propagating room temperature synthesis of nanopowders for solid oxide fuel cells (SOFC). *J. Power Sources* **2005**, *145*, 237−242.
(29) Zhou, X.-D.; Huebner, W. Size-induced lattice relaxation in CeO_2 nanoparticles. *Appl. Phys. Lett.* **2001**, *79*, 3512−3514.
(30) Lowell, S. *Characterization of Porous Solids and Powders: Surface Area, Pore Size and Density*; Kluwer Academic Publishers: Dordrecht, The Netherlands, 2004.
(31) Jia, T.-J.; Song, G.; Li, P.-W.; He, T.-C.; Mo, Y.-J.; Cui, Y.-T. Vibrational modes study of methyl orange using SERS-measurement and the DFT method. *Mod. Phys. Lett. B* **2008**, *22*, 2869−2879.
(32) Sathiyabama, J.; Rajendran, S.; Selvi, J. A.; Amalraj, A. J. Methyl orange as corrosion inhibitor for carbon steel in well water. *Indian J. Chem. Technol.* **2008**, *15*, 462−466.
(33) Liu, Y.; Sun, D. Z. Development of Fe_2O_3-CeO_2-TiO_2/gamma-Al_2O_3 as catalyst for catalytic wet air oxidation of methyl orange azo dye under room condition. *Appl. Catal., B* **2007**, *72*, 205−211.
(34) Hua, Q.; Shi, F. C.; Chen, K.; Chang, S. J.; Ma, Y. S.; Jiang, Z. Q.; Pan, G. Q.; Huang, W. X. Cu_2O-Au nanocomposites with novel structures and remarkable chemisorption capacity and photocatalytic activity. *Nano Res.* **2011**, *4*, 948−962.
(35) Telke, A. A.; Kalyani, D. C.; Dawkar, V. V.; Govindwar, S. P. Influence of organic and inorganic compounds on oxidoreductive decolorization of sulfonated azo dye CI Reactive Orange 16. *J. Hazard. Mater.* **2009**, *172*, 298−309.
(36) Galindo, C.; Jacques, P.; Kalt, A. Photodegradation of the aminoazobenzene acid orange 52 by three advanced oxidation processes: UV/H_2O_2 UV/TiO_2 and VIS/TiO_2 - Comparative mechanistic and kinetic investigations. *J. Photochem. Photobiol., A* **2000**, *130*, 35−47.
(37) Yue, L.; Zhang, X.-M. Structural characterization and photocatalytic behaviors of doped CeO2 nanoparticles. *J. Alloys Compd.* **2009**, *475*, 702−705.
(38) Danish, M.; Hashim, R.; Ibrahim, M. N. M.; Sulaiman, O. Characterization of physically activated acacia mangium wood-based carbon for the removal of methyl orange dye. *BioResources* **2013**, *8*, 16.
(39) Dohčević-Mitrović, Z. D.; Šćepanović, M. J.; Grujić-Brojčin, M. U.; Popović, Z. V.; Bošković, S. B.; Matović, B. M.; Zinkevich, M. V.; Aldinger, F. The size and strain effects on the Raman spectra of $Ce_{1-x}Nd_xO_{2-d}$ ($0 \leq x \leq 0.25$) nanopowders. *Solid State Commun.* **2006**, *137*, 387−390.
(40) Deacon, G. B.; Phillips, R. J. Relationships between the carbon-oxygen stretching frequencies of carboxylato complexes and the type of carboxylate coordination. *Coord. Chem. Rev.* **1980**, *33*, 227−250.
(41) Bauer, C.; Jacques, P.; Kalt, A. Investigation of the interaction between a sulfonated azo dye (AO7) and a TiO_2 surface. *Chem. Phys. Lett.* **1999**, *307*, 397−406.
(42) Yang, Z.; Wang, Q.; Wei, S.; Ma, D.; Sun, Q. The effect of environment on the reaction of water on the ceria(111) surface: A DFT+U study. *J. Phys. Chem. C* **2010**, *114*, 14891−14899.
(43) Kundakovic, L.; Mullins, D. R.; Overbury, S. H. Adsorption and reaction of H_2O and CO on oxidized and reduced Rh/CeO_x(111) surfaces. *Surf. Sci.* **2000**, *457*, 51−62.
(44) Lima, E. C.; Royer, B.; Vaghetti, J. C. P.; Simon, N. M.; da Cunha, B. M.; Pavan, F. A.; Benvenutti, E. V.; Cataluña-Veses, R.; Airoldi, C. Application of Brazilian pine-fruit shell as a biosorbent to removal of reactive red 194 textile dye from aqueous solution: Kinetics and equilibrium study. *J. Hazard. Mater.* **2008**, *155*, 536−550.
(45) Tseng, R.-L.; Wu, F.-C. Inferring the favorable adsorption level and the concurrent multi-stage process with the Freundlich constant. *J. Hazard. Mater.* **2008**, *155*, 277−287.
(46) Zhu, Y.-P.; Liu, Y.-L.; Ren, T.-Z.; Yuan, Z.-Y. Hollow manganese phosphonate microspheres with hierarchical porosity for efficient adsorption and separation. *Nanoscale* **2014**, *6*, 6627−6636.
(47) Yeddou-Mezenner, N. Kinetics and mechanism of dye biosorption onto an untreated antibiotic waste. *Desalination* **2010**, *262*, 251−259.